Supplementary information

Confined antiskyrmion motion driven by electric current excitations

Yao Guang*, Xichao Zhang, Yizhou Liu, Licong Peng, Fehmi Sami Yasin, Kosuke Karube,

Daisuke Nakamura, Naoto Nagaosa, Yasujiro Taguchi, Masahito Mochizuki, Yoshinori

Tokura, Xiuzhen Yu*

Contents:

Note 1. Device fabrication and pulse current source output

Note 2. Pulse-width effect on the antiskyrmion motion

Note 3. The motion of an antiskyrmion and a half-antiskyrmion pair (HAP) in a stripe with $j \parallel$ H-Str

Note 4. The motion of an elongated antiskyrmion under field reversals in the $j \parallel$ H-Str

Note 5. The motion of an elongated antiskyrmion in the $j \perp$ V-Str

Note 6. An elongated antiskyrmion ($n = 3$) dynamics with current reversals

Note 7. Micromagnetic simulations for an elongated antiskyrmion ($n = 3$) in both $j \parallel$ H-Str and $j \perp$ V-Str directions

Note 8. Changes of antiskyrmion shape with critical stimulations

Note 9. Effect of external field on the antiskyrmion motion in $j \perp$ V-Str

Note 10. Current driven isolated antiskyrmion in a ferromagnetic background

Note 11. Topological charge calculation of the antiskyrmion and HAP by micromagnetic simulation

Note 12. The motion of an antiskyrmion in a stripe with $j \perp$ V-Str

Note 13. Effect of external field on the HAP motion in $j \perp$ V-Str

Note 1. Device fabrication and pulse current source output.

The two terminal devices in this study were fabricated using the focused ion beam (FIB) technique to investigate current-driven dynamics of spin textures. The $(Fe_{0.63}Ni_{0.3}Pd_{0.07})_3P$ (FNPP) plates in the devices were cut from the bulky FNPP and thinned to the desired thickness of approximately 160 nm to stabilize antiskyrmion textures[1,2]. The Curie temperature of FNPP thin plates with a thickness of 160 nm is approximately 440 K[2], which ensures our Lorentz transmission electron microscopy (LTEM) observations of spin textures at room temperature. The two ends of FNPP plates were coated with tungsten (W) and fixed to the two terminals of an E-chip (E-FEF01-A2, Protochips), as illustrated in Fig. S1 (a).

The data on current-driven spin textures presented in this study were obtained from two devices: Device 1 with dimensions of 0.16 μm ×4.9 μm × 6 μm and Device 2 with dimensions of 0.16 μm × 4.3 μm × 2.5 μm, as shown in Figs. S1b and S1c, respectively. The data of Figs. 2d, 2e, 2g, 2h, 2k, 2n, 3, 4, S1b, S3, S6, S7b, S9b, S10, S12b, S15, and S16 in this manuscript are obtained from device 1. The data of Figs. 2i, 2m, S1c, S2, S4, S5, S7a, S9a, S12a, and S13 in this manuscript are obtained from device 2. The horizontal and vertical directions are denoted as $x \parallel [1\bar{1}0]$ and $y \parallel [110]$. The current flows through devices along the x-axis, and the pulse width was kept at 50 ns, as depicted in Fig. S1 (d).
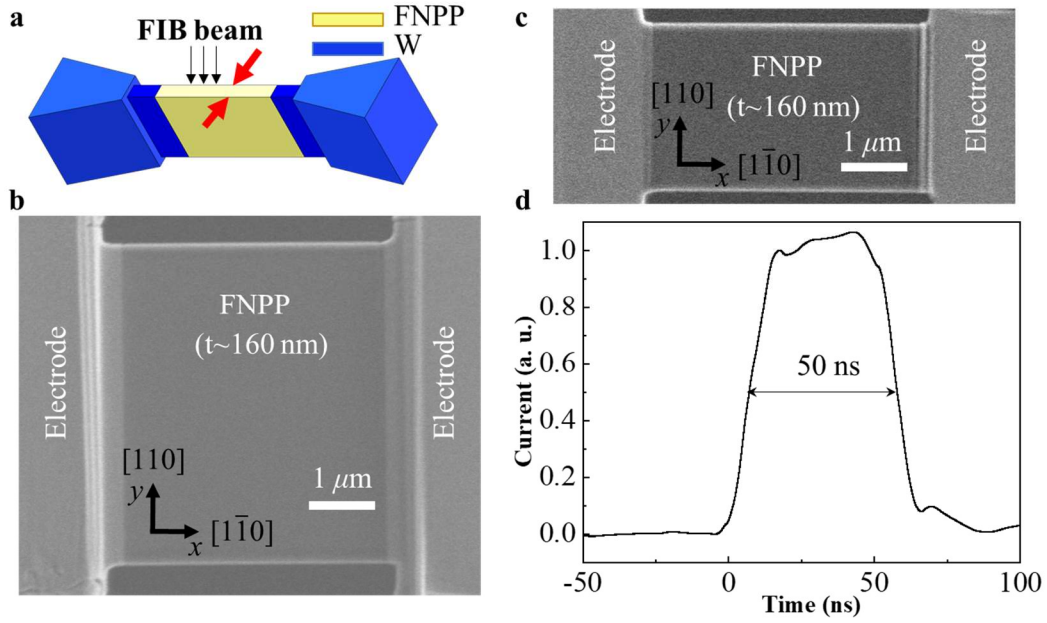
Fig. S1 | Device forms and the configuration of the pulse current. **a**, Scheme of the two-terminal device fabrication with the focused ion beam. **b**, **c**, The SEM images of Device 1 (b) and Device 2 (c). **d**, The current profile applied on the two terminal devices with 50 ns pulse width. The scale bar in **b** and **c** is 1 μm.

Note 2. Pulse-width effect on the antiskyrmion motion

We obtain a pulse-width dependence of the critical current density j_c for driving antiskyrmions to comprehend the influence of pulse width on antiskyrmion dynamics. Figure S2 shows that $|j_c|$ decreases nonlinearly with increases of the pulse width Δt as j $\parallel$ H-Str. This trend in the dependence of critical current density on pulse width is reminiscent of the behavior observed in skyrmion-flow motion in $Co_9Zn_9Mn_2$[3]. On the other hand, a Joule heating effect on spin textures, such as heat-induced transformations and annihilations of spin textures, becomes pronounced when Δt exceeds approximately 1 ms. Therefore, using short pulse widths can effectively mitigate Joule heating and demonstrate the spin-transfer torque (STT) effect in current-driven
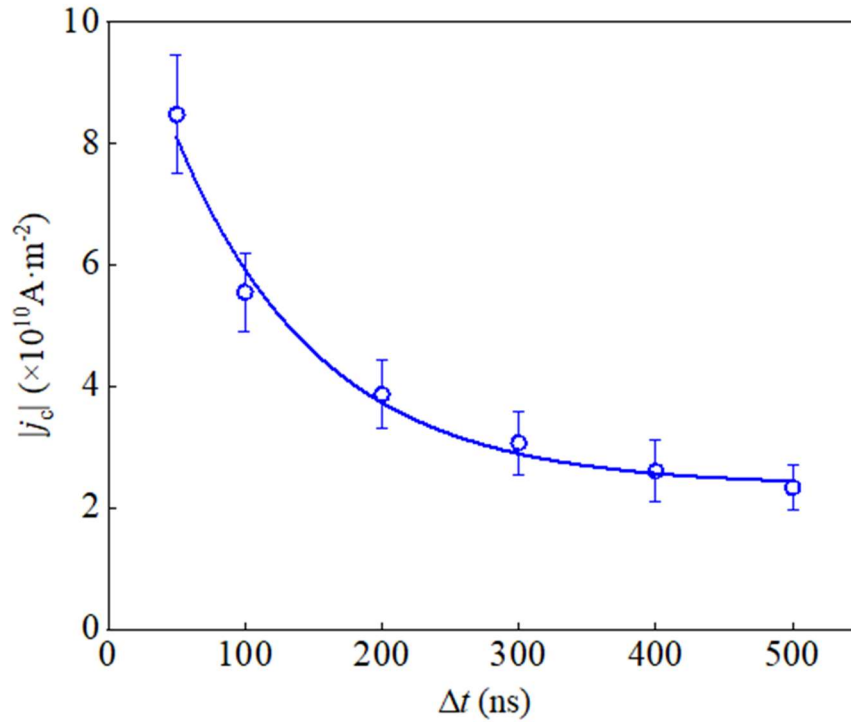
antiskyrmion dynamics.

Fig. S2 | Pulse width dependence of critical current density to drive antiskyrmion. The solid line represents the exponential decay fitting curve, and the data points are shown as circles. The error bars in the plot represent the standard deviation from the mean of multiple trails.

We have conducted quantitative experiments to study elongated antiskyrmions (n = 4) with varying pulse widths at a fixed current density $j = 0.78 \times 10^{11}$ A m^{-2} (Fig. S3a) applied in $j \parallel$ H-Str and $j = -0.59 \times 10^{11}$ A m^{-2} (Fig. S3b) applied in $j \perp$ V-Str. The results indicate that elongated antiskyrmions exhibit a non-linear increase with increasing pulse width in both the $j \parallel$ H-Str and $j \perp$ V-Str cases. Supplementary Movie 1 and Supplementary Movie 2 show the elongated antiskrymion (n = 4) under 90 ns pulse width in $j \parallel$ H-Str and $j \perp$ V-Str, respectively. When a pulse width of 110 ns is applied

parallel to H-Str configuration, the elongated antiskyrmion becomes highly unstable, transforming into non-topological bubbles and ultimately annihilating, as shown in Supplementary Movie 3. Semiseriously, the H-Str fractures at this pulse width. Similarly, the transformation also occurs for the elongated antiskyrmion ($n = 4$) in $j \perp$ V-Str with a 150 ns pulse width, as shown in Supplementary Movie 4. These results indicate that increasing the pulse width results in a non-linear increase in the antiskyrmion velocity, while also enhancing the Joule heating effect, potentially leading to the breakdown of antiskyrmions and stripe domains.
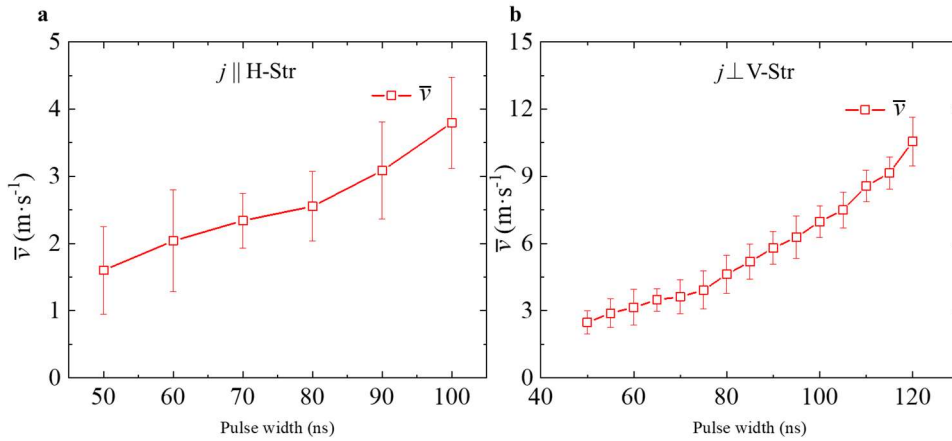

Fig. S3 | Pulse width dependence of antiskyrmion ($n = 4$) velocity in both $j \parallel$ H-Str and $j \perp$ V-Str

a, Pulse width dependence of antiskyrmion ($n = 4$) velocity in $j \parallel$ H-Str at $j = 0.78 \times 10^{11}$ A m^{-2}. **b**, Pulse width dependence of antiskyrmion ($n = 4$) velocity in $j \perp$ V-Str at $j = -0.59 \times 10^{11}$ A m^{-2}. The error bars in the plots represent the standard deviation from the mean of multiple trails.

Note 3 The motion of an antiskyrmion and a half-antiskyrmion pair (HAP) in a stripe with $j \parallel$ H-Str

The current-driven motion of both antiskyrmion and HAP along a single stripe are examined, as illustrated in Fig. S4. The antiskyrmion and HAP are highlighted with red and blue rectangular dashed lines, respectively. To characterize the response of antiskyrmion and HAP, we maintain a fixed pulse width of 50 ns while gradually increasing the current density from zero to $1.60 \times 10^{11} \mathrm{A \cdot m^{-2}}$. The left and right panels in Fig. S4a display LTEM images with pulse-current stimulations in opposite directions while keeping $|j| = 1.20 \times 10^{11} \mathrm{A \cdot m^{-2}}$. The antiskyrmion and HAP do not move when $j = 1.20 \times 10^{11} \mathrm{A \cdot m^{-2}}$ flows through a single stripe of H-Str. Notably, a significant change in spin textures occurred upon increasing j to $1.45 \times 10^{11} \mathrm{A \cdot m^{-2}}$, causing the H-Str at the left boundary to transform partially into V-Str, and further increasing j to $1.60 \times 10^{11} \mathrm{A \cdot m^{-2}}$ (as shown in Fig. S4b) results in the motion of antiskyrmion regardless of the current direction parallel or antiparallel to the x-axis, which indicates that the boundary condition is essential to affect the antiskyrmion dynamics. The HAP eventually transformed and disappeared after the fourth pulse-current stimulation, suggesting that the spin texture becomes unstable under higher current densities, possibly due to the larger Joule heating.
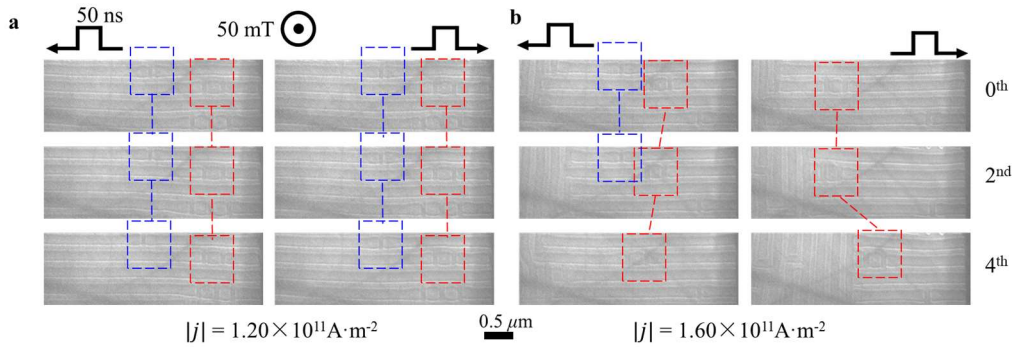

Fig. S4 | Current-driven an antiskyrmion and a half-antiskyrmion pair (HAP) in a single stripe with $j \parallel$ H-Str. a, b Representative LTEM images showing current-

driven an antiskyrmion (**a**) and a HAP (**b**) motions by pulse current stimulating under +50 mT field, respectively. The rectangular frames with blue and red lines marked the HAP and antiskyrmion, respectively. The scale bar for images in **a** and **b** is 0.5 μm.

Note 4. The motion of elongated antiskyrmion under field reversals in the $j \parallel$ H-Str

Since driving an antiskyrmion by currents in a single strip domain is challenging as the $j \parallel$ H-Str, our focus shifts to estimating the motion of elongated antiskyrmions with the current $j \parallel$ H-Str. Figures S5a and S5b show the average velocity of antiskyrmions as a function of current density for $n = 2$ and $n = 3$ under magnetic fields of −50 mT and 50 mT, respectively. Notably, the motion of antiskyrmion consistently aligns parallel to the direction of the current flow, even when the external magnetic field is reversed. These results underscore the intrinsic topological characteristics of antiskyrmions. According to the defined equation, the topological charge (Q) of antiskyrmion should be +1 at −50 mT, leading to the core magnetization of the antiskyrmion being antiparallel to the external magnetic field. Conversely, the field reversal should result in its topological charge $Q = -1$ at +50 mT. The moving direction of antiskyrmions is determined by the spin polarization of the conduction electrons, which is directly associated with the core magnetizations.
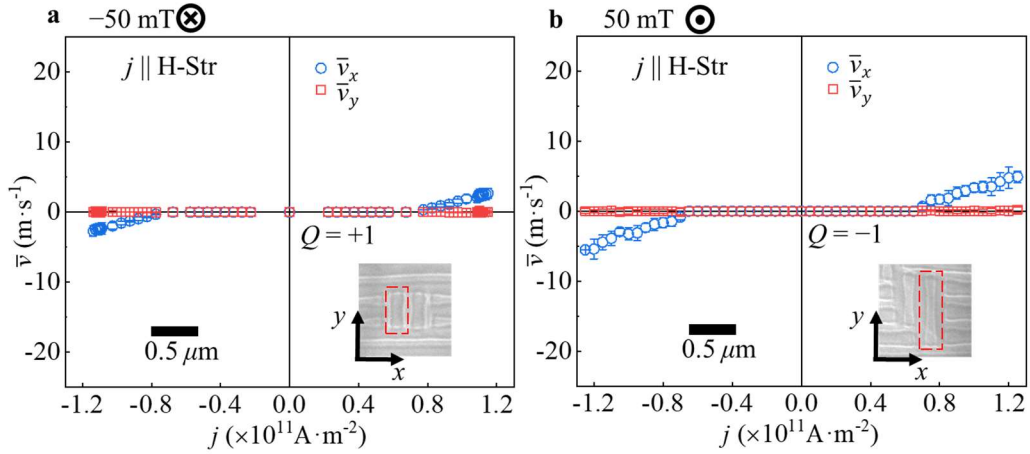
Fig. S5 | Current driven elongated antiskyrmion with _j_ ∥ H-Str. a,b, Average velocity of elongated antiskyrmion versus current density under −50 mT (**a**) and +50 mT (**b**), respectively. The error bars in the plots represent the standard deviation from the mean of multiple trails. The scale bar for inset images in **a** and **b** is 0.5 μm.

Note 5. The motion of an elongated antiskyrmion in the _j_ ⊥ V-Str

During our experiments, we observed that elongated antiskyrmion can be formed using the same creation procedure as that for the antiskyrmion formation. Considering that the elongation of an antiskyrmion may also have significant implications on its motion, we created several antiskyrmions with different lengths, defined by a ratio _n_ of the antiskyrmion length and helical period, and then investigated the motions of antiskyrmions. As depicted in Fig. S6, the results present the average velocity of antiskyrmions as a function of current density for _n_ = 2 under a magnetic field of –50 mT.
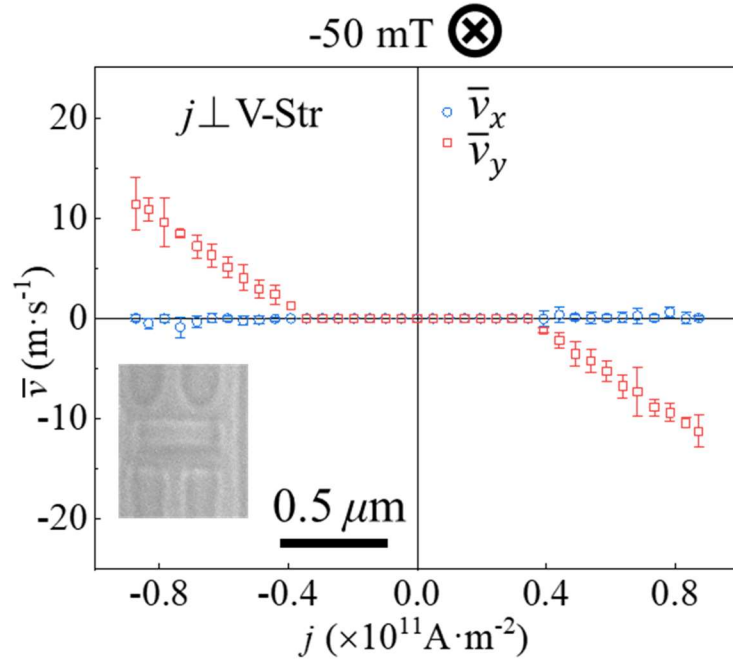
Fig. S6 | Current driven elongated antiskyrmion with $j \perp$ V-Str. Average velocity of elongated antiskyrmion versus current density for $n = 2$ under −50 mT. The error bars in the plot represent the standard deviation from the mean of multiple trails. The scale bar for the inset image is 0.5 μm.

Note 6. An elongated antiskyrmion ($n = 3$) with current reversals.

To demonstrate the reversibility of antiskyrmion dynamics as depicted in Fig 2i and 2k, we conducted experiments involving elongated antiskyrmions ($n = 3$) with current reversals in both $j \parallel$ H-Str and $j \perp$ V-Str configuration, as shown in Fig. S7a and Fig. S7b, respectively.
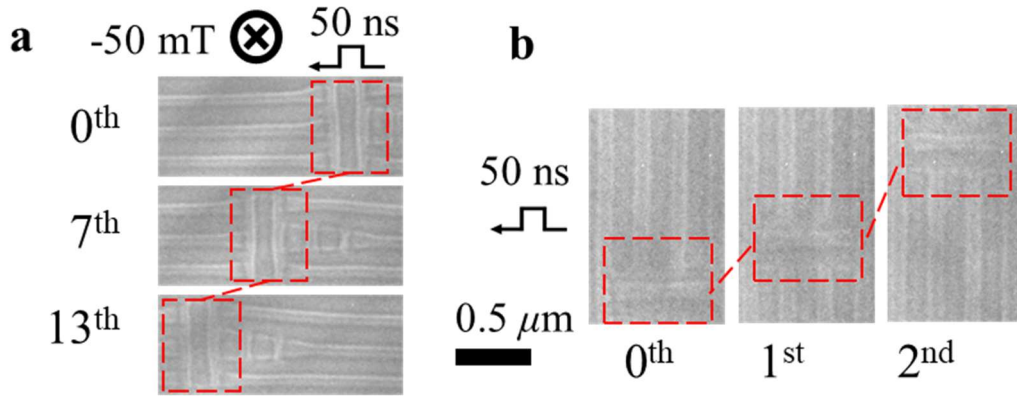
Fig. S7 | Elongated antiskyrmion (*n* = 3) with current reversals at –50 mT. a, **b**, LTEM images were observed after sequential current pulse applications showing the current-driven antiskyrmion (marked by the red rectangular dashed line) motion in H-Str (**a**) and in V-Str (**b**) for negative current. The scale bar for images in **a** and **b** is 0.5 μm.

Note 7. Micromagnetic simulations for an elongated antiskyrmion (*n* = 3) in both *j* ∥ H-Str and *j* ⊥ V-Str directions.

To better understand the dynamics of elongated antiskyrmions, we conducted micromagnetic simulations for an elongated antiskyrmion (*n* = 3) in comparison with our experimental results depicted in Fig. 2m and 2n in the main text, as illustrated in Fig. S8. The simulation results are consistent with our experimental findings in Fig. 2m and 2n, suggesting that a device based on the V-Str geometry could be more energy efficient.
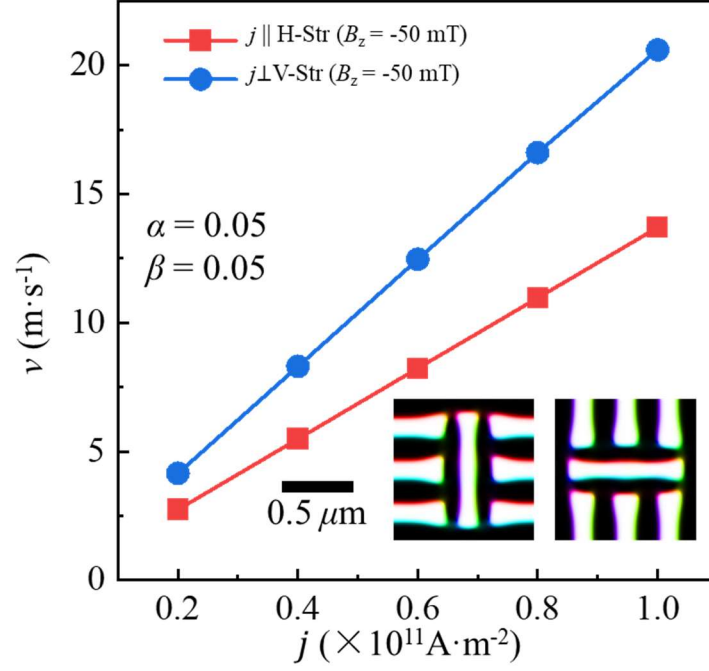
Fig. S8 | Velocity dependence of elongated antiskyrmion ($n = 3$) on current density. The red solid square and blue solid circle represent data points of elongated antiskyrmions in $j \parallel$ H-Str and $j \perp$ V-Str, respectively. The solid lines represent the linear fitting curves of the corresponding data points. The scale bar for inset images in is 0.5 μm.

Note 8. Changes of antiskyrmion shape with critical stimulations.

Based on our experimental findings, we have observed a strong dependence of antiskyrmion dynamics on the elongation number of the antiskyrmion. To elucidate this relationship, we present a summary of the data concerning the critical current density for elongated antiskyrmions ($n = 1$, 2, and 3) in both current flow parallel H-Str and perpendicular to the V-Str at −50 mT, as is shown in Fig. S9. Regardless of the current flow parallel or perpendicular to the stripe direction, we observe a reduction in the critical current density with an increase in the elongation number. This indicates that antiskyrmions in $j \perp$ V-Str are more easily driven by current compared to those in $j \parallel$ H-

Str. Notably, squared antiskyrmions require nearly twice the strength of current density to driven the antiskyrmion motions in $j \parallel$ H-Str compared to $j \perp$ V-Str, while the required current density for the squared antiskyrmion annihilation remains approximately the same. Furthermore, the critical current density tends to stabilize as the elongation number increases.
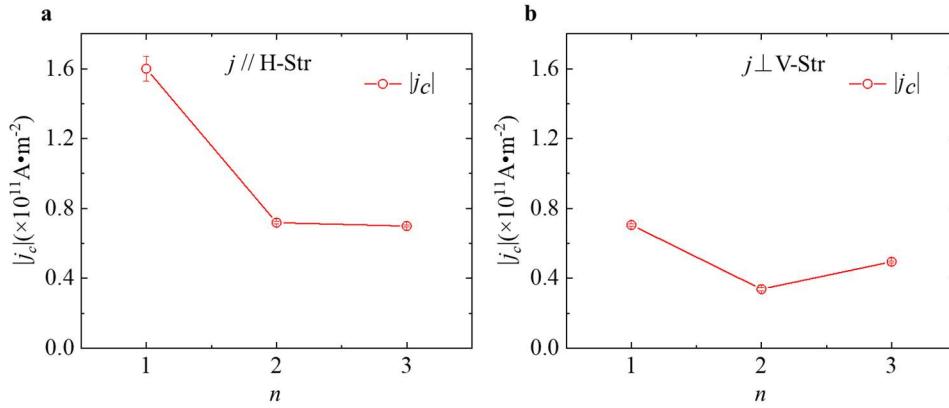

Fig. S9 | The influence of antiskyrmion shape on critical driven current density.

a, **b**, Critical current density in $j \parallel$ H-Str and $j \perp$ V-Str, respectively, for driving the antiskyrmion with $n = 1$, 2, and 3. The error bars in the plots represent the standard deviation from the mean of multiple trails.

Note 9. Effect of external field on the antiskyrmion motion in $j \perp$ V-Str

To investigate the field effect on the elongated aiskyrmion dynamics within the $j \perp$ V-Str, we conduct the elongated antiskyrmions with $n = 3$ by varying the current density under several fields of 0 mT, −50 mT, and −100 mT. Figures S10a and S10b illustrate the average velocity of an antiskyrmion versus current density at 0 mT and −100 mT, respectively.
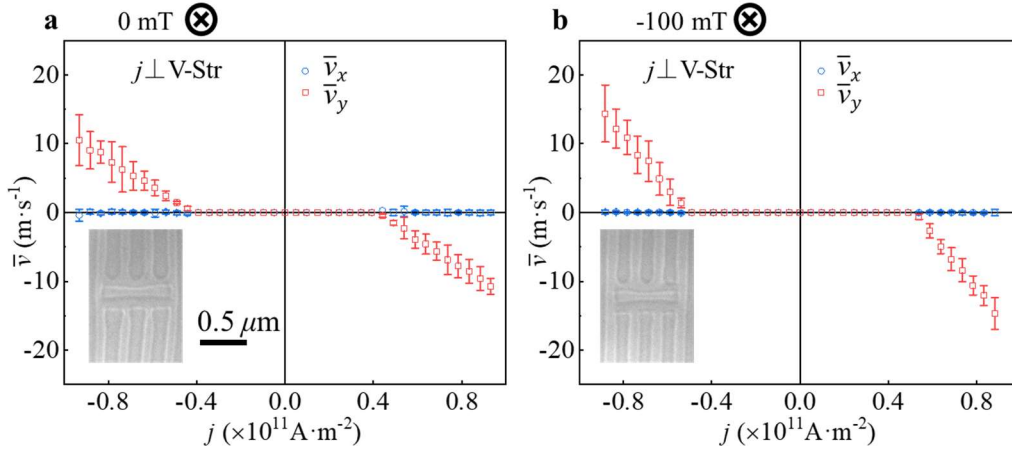
Fig. S10 | Current driven elongated antiskyrmion with $j \perp$ V-Str under different fields. **a,b**, Average velocity of an elongated antiskyrmion ($n = 3$) versus current density at 0 mT (a) and -100 mT (b). The error bars in the plots represent the standard deviation from the mean of multiple trails. The scale bar for inset images in **a** and **b** is 0.5 μm.

We have also performed micromagnetic simulations for current-driven squared antiskyrmion ($n = 1$) at -100 mT. In Fig. S11, it is evident that the velocity of the squared antiskyrmion at -100 mT shows a significant 15% enhancement compared to -50 mT in $j \perp$ V-Str, while the velocity of the squared antiskyrmion at -100 mT remains unchanged compared to -50 mT in $j \parallel$ H-Str.
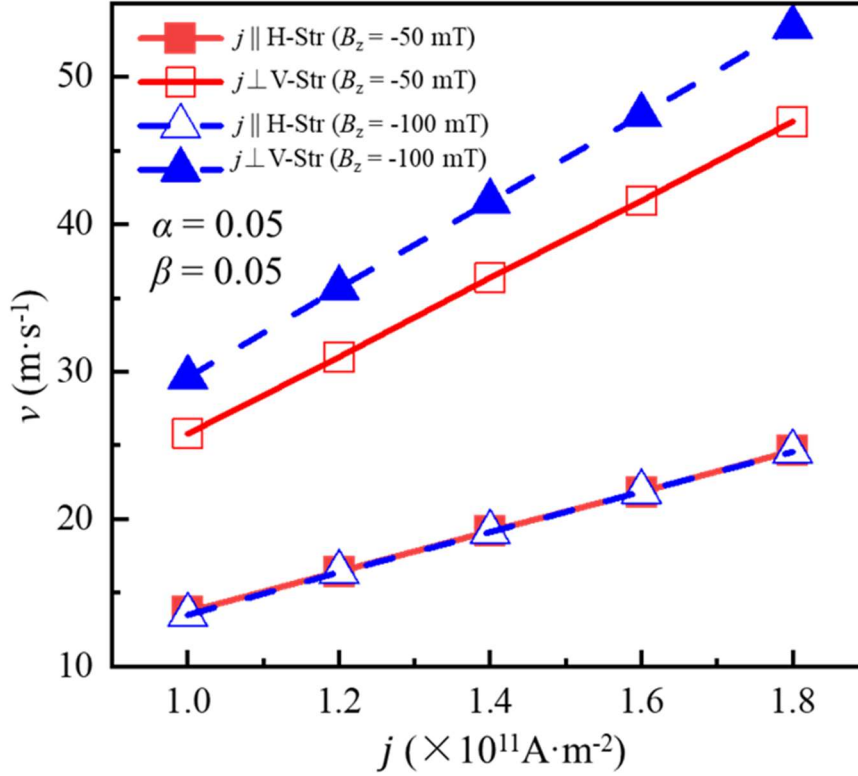
Fig. S11 | Simulation results of velocity of a squared antiskyrmion dependence with varying field. Velocity of squared antiskyrmion ($n = 1$) versus current density at -50 mT (red solid line), and -100 mT (blue dashed line). The red solid square, blue blank triangle represents data points in $j \parallel$ H-Str. The red blank square, blue solid triangle represents data points in $j \perp$ V-Str.

Additionally, we have observed that the elongated antiskyrmion ($n = 3$) becomes unstable at -150 mT under both current flow parallel H-Str and perpendicular to the V-Str. This instability is illustrated in Fig. S12, where the elongated antiskyrmion in $j \parallel$ H-Str and $j \perp$ V-Str transform into non-topological bubble at the second pulse (Fig. S12a) and first pulse (Fig. S12b), respectively.

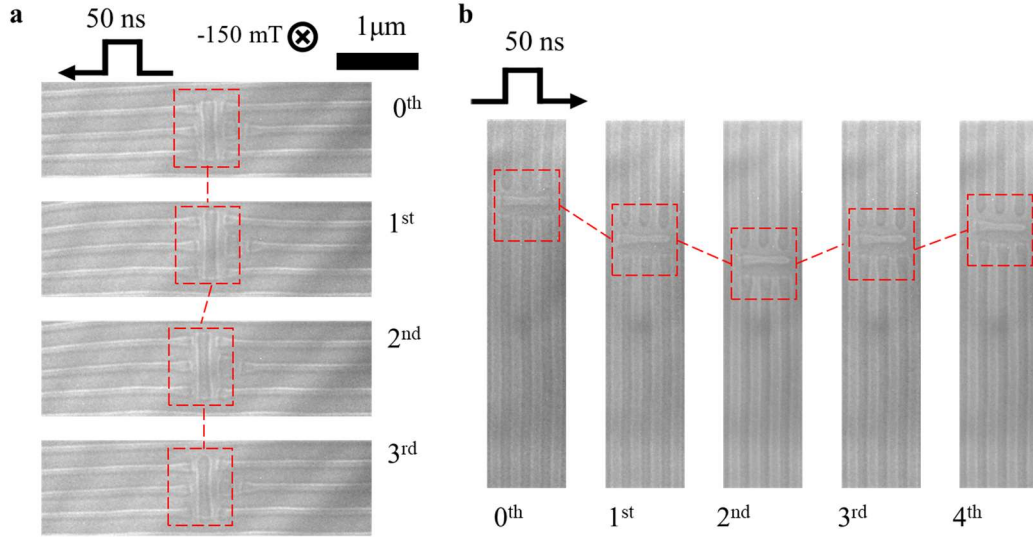**Fig. S12 | Current-driven an elongated antiskyrmion ($n = 3$) at -150 mT.**

a, b Representative LTEM images showing current-driven an elongated antiskyrmion dynamics in $j \parallel$ H-Str **(a)** at $j = -0.90 \times 10^{11}$ A·m^{-2} and $j \perp$ V-Str **(b)** at $j = 0.97 \times 10^{11}$ A·m^{-2}, respectively. The scale bar for images in **a** and **b** is 1 μm.

Note 10. Current driven isolated antiskyrmion in a ferromagnetic background.

We have also attempted to understand the differences of antiskyrmion dynamic behavior between the helical and the ferromagnetic background under pulse current stimulation. As shown in Fig. S13a, the metastable isolated antiskyrmion exhibits considerable instability. Following a small pulse of current density ($j = -0.50 \times 10^{11}$ A m^{-2}), the antiskyrmion undergoes transformation into a non-topological bubble without displacement, as illustrated in Fig. S13b.
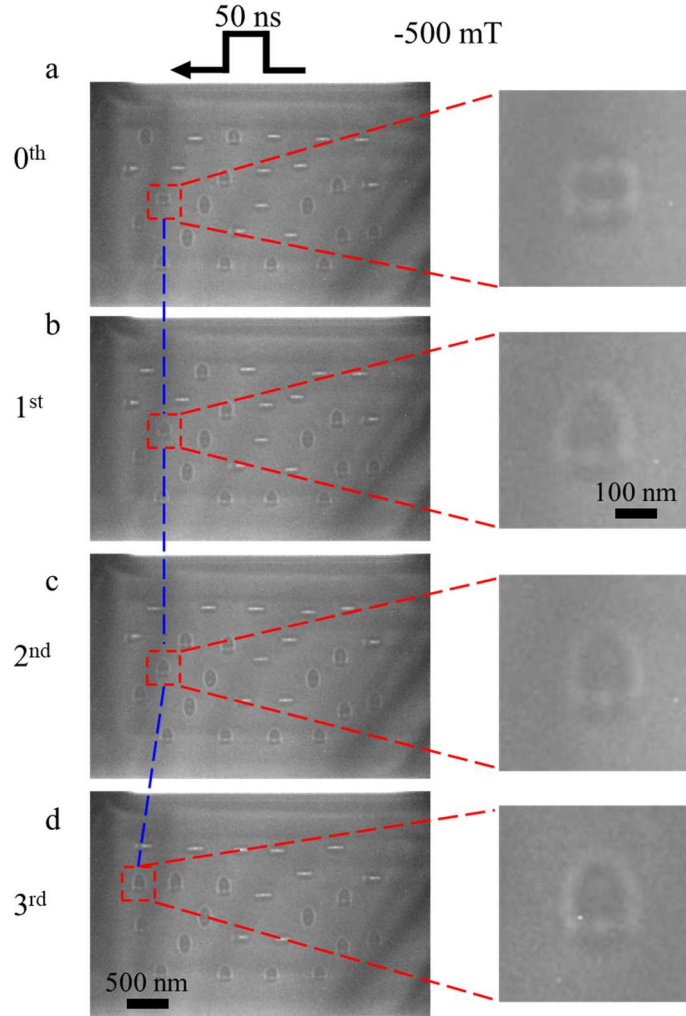
Fig. S13 | Isolated antiskyrmion dynamics in ferromagnetic background.

a-d, Sequence of LTEM images after a 50 ns width pulse at −500 mT with $j = -0.50 \times 10^{11}$ A m^{-2}. The blue dashed line serves as a guideline for tracking the initial antiskyrmion after each pulse. The right side corresponds to a zoomed-in view of the region enclosed by the red dashed square. The scale bar for images in **a**, **b**, **c**, and **d** is 500 nm. The scale bar for the zoom-in region images is 100 nm.

Note 11. Topological charge calculation of the antiskyrmion and HAP by micromagnetic simulation

To better comprehend the topology of antiskyrmions and HAP, we conducted

micromagnetic simulations to calculate their topological charges. As illustrated in Figs. S14a and S14b, the rectangular regions highlighted with cyan dashed lines represent the antiskyrmion and HAP, respectively. The corresponding topological charge calculations within these dashed line regions yielded $Q = +1$ for both the antiskyrmion and HAP. However, we point out that the sign of Q also depends on the orientation of the background magnetization; nevertheless, both the antiskyrmion and HAP carry an identical vorticity number of -1, which is independent of the background magnetization orientation.
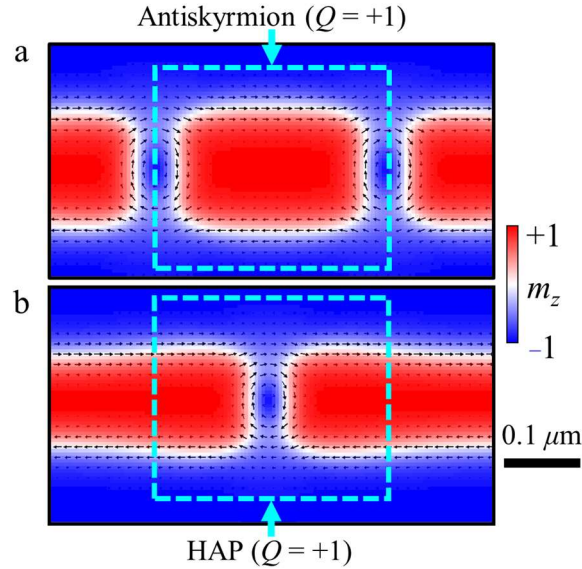

Fig. S14 | Topological charge calculation of the antiskyrmion and HAP by using micromagnetic simulation. The topological charge of the antiskyrmion (a) and the HAP (b) within the rectangular regions outlined by cyan dashed lines is identical, i.e., $Q = +1$. The antiskyrmion and HAP also carry an identical vorticity number of -1. The scale bar for images in **a** and **b** is 0.1 μm.

Note 12. The motions of an antiskyrmion in a stripe domain with $j \perp$ V-Str

To investigate the changes in current-driven antiskyrmion dynamics with respect to the current direction along H-Str ($j \parallel$ H-Str) and perpendicular to V-Str ($j \perp$ V-Str),

we assessed the motion of an antiskyrmion along a single stripe while varying the pulse current density, as shown in Figs. 4c and 4d. Besides, we also observed the antiskyrmion elongated behavior during their motion at the $|j| = 0.78\times10^{11}A\cdot m^{-2}$, as illustrated in Fig. S15.
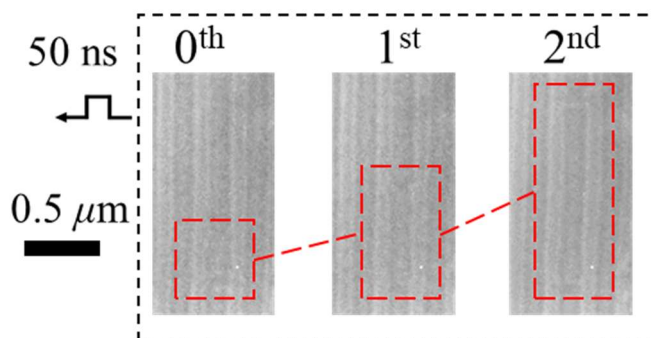

Fig. S15 | Current-driven an antiskyrmion in a single stripe domain with $j \perp$ V-Str. Representative LTEM images of current-driven an antiskyrmion in a single stripe at $|j| = 0.78\times10^{11}A\cdot m^{-2}$ under −50 mT. The scale bar is 0.5 μm.

Note 13. Effect of external field on the HAP motion in $j \perp$ V-Str

While investigating the motion of HAP within the $j \perp$ V-Str, we observed that it exhibits greater mobility compared to that driven by the $j \mathbin{\!/\mkern-5mu/\!}$ H-Str. In addition to conducting the experiment at a magnetic field of −50 mT, as depicted in Fig. 4, we also performed LTEM observations of HAP motions at 0 mT and −100 mT. As shown in Figs. S16a and S16b, we analyzed the average velocity of HAP as a function of current density at 0 mT and -100 mT, respectively.

When the j is fixed at 0.69 A·m⁻², the average velocity at 0 mT, −50 mT, and −100 mT is found to be 15.2 m s⁻¹, 12.8 m s⁻¹, and 7.6 m s⁻¹, respectively. These results suggest that the current-driven motion of HAP is suppressed at higher magnetic fields when j $\perp$ V-Str. Furthermore, HAP also becomes unstable at higher magnetic fields, such as
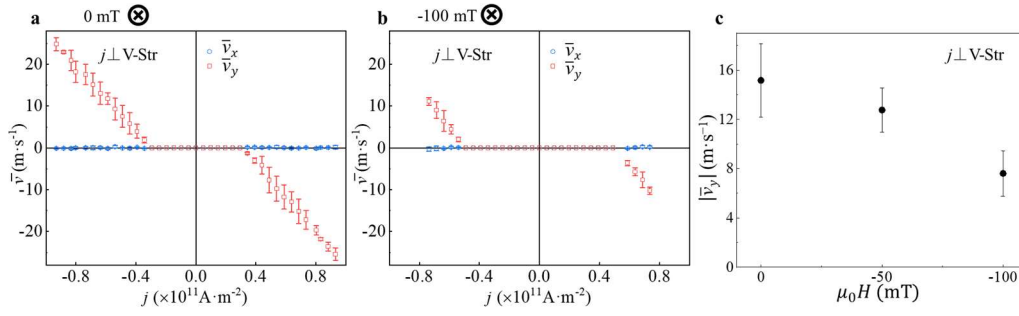
100 mT, leading to the annihilation of HAP.

Fig. S16 | Current-driven HAP with $j \perp$ V-Str under different fields. a,b, The average velocity of elongated antiskyrmion versus current density under 0 mT (a) and -100 mT (b). **c**, The average velocity of HAP versus external field at $j = 0.69 \times 10^{11} \text{A·m}^{-2}$. The error bars in the plot represent the standard deviation from the mean of multiple trails.

References

1   Karube, K. *et al.* Room-temperature antiskyrmions and sawtooth surface textures in a non-centrosymmetric magnet with S4 symmetry. *Nat. Mater.* **20**, 335-340 (2021).

2   Peng, L. *et al.* Formation and control of zero-field antiskyrmions in confining geometries. *Adv Sci* **9**, e2202950 (2022).

3   Peng, L. *et al.* Dynamic transition of current-driven single-skyrmion motion in a room-temperature chiral-lattice magnet. *Nat. Commun.* **12**, 6797 (2021).